Submicrometer tomography of cells by multiple-wavelength digital holographic microscopy in reflection

Jonas Kühn,[1,*] Frédéric Montfort,[2] Tristan Colomb,[2] Benjamin Rappaz,[3] Corinne Moratal,[3] Nicolas Pavillon,[1] Pierre Marquet,[3] and Christian Depeursinge[1]

[1]*Institute of Imaging and Applied Optics, Ecole Polytechnique Fédérale de Lausanne, CH-1015 Lausanne, Switzerland*

[2]*Lyncée Tec SA, PSE-A, CH-1015 Lausanne, Switzerland*

[3]*Brain Mind Institute, Ecole Polytechnique Fédérale de Lausanne, CH-1015 Lausanne, Switzerland*

[*]*Corresponding author: jonas.kuehn@a3.epfl.ch*

Received November 10, 2008; revised January 15, 2009; accepted January 16, 2009; posted January 27, 2009 (Doc. ID 103859); published February 25, 2009

We present first results on a method enabling mechanical scanning-free tomography with submicrometer axial resolution by multiple-wavelength digital holographic microscopy. By sequentially acquiring reflection holograms and summing 20 wavefronts equally spaced in spatial frequency in the 485–670 nm range, we are able to achieve a slice-by-slice tomographic reconstruction with a 0.6–1 μm axial resolution in a biological medium. The method is applied to erythrocytes investigation to retrieve the cellular membrane profile in three dimensions. © 2009 Optical Society of America

OCIS codes: 090.1995, 110.0180, 110.6955, 170.6960.

Digital holographic microscopy (DHM) is a recent interferometric technique providing full-field complex object wavefront retrieval with an acquisition rate mainly limited by the camera. A vast field of application concerns cellular biology, from neuron imaging [1] and red blood cell analysis [2,3] to cancerous cell screening [4]. In all these approaches, the phase signal provided by DHM is obtained in a transmission configuration and is proportional to the integrated optical path length (OPL) along the optical axis through the specimen, dependent on both topology and mean intracellular refractive index. Although methods to decouple both variables exist [5,6], the measurement remains an integrated value; consequently no precise interface or subcellular component localization is possible in the axial z direction.

In the past few years, multiple angles digital holographic tomography and tomographic phase microscopy have rapidly evolved to recover a full-three-dimensional (3D) refractive index map of intracellular structures. Nevertheless, all these techniques rely on some mechanical scanning, either by rotating the objet [7] or varying the illumination beam angle [8,9]. We use here a wavelength-scanned method; thus neither the object nor any part of the setup is mechanically moved. The principle is based on multiple-wavelength digital holographic tomography [10–12], where different equally k-spaced-wavelengths full-field holograms are sequentially acquired, and corresponding wavefronts are summed in order to add constructively in a plane of interest in which they are in phase and destructively in out-of-plane regions (slicing effect). Instead of the usual thick tissue or reflective specimen investigated in these previous works, we present a new approach enabling us to retrieve the reflection phase signal of fixed red blood cells (RBCs) for which the membrane geometry in 3D is retrieved thanks to the submicrometer resolution of our experimental configuration.

This tomography method, a refined version of the one in [11], relies on the addition principle, where several backscattered electric fields at different wavelengths are superposed to obtain the optical sectioning effect. Indeed, if we measure at an arbitrary point Q the field originating from an object point P with an amplitude A inside a sample volume V, neglecting $1/r$ amplitude dependence for high-NA microscopy, and if we do that for N wavelengths in the $[k_{\min}, k_{\max}]$ range, with $\bar{k}=1/N\Sigma k_j$, we get the expression of Eq. (1) [11],

$$\Psi(Q) \propto \int_V A(P) e^{i\bar{k} r_{PQ}} T(r_{PQ}) \mathrm{d}^3 \mathbf{r}_{PQ}, \tag{1}$$

with $r_{PQ}=n_m|\mathbf{r}_P-\mathbf{r}_Q|$ as the OPL between P and Q in a medium refractive index n_m.

In Eq. (1), the term $T(r_{PQ})$ is an amplitude filter function or "z-slicing function," which attenuates out-of-plane contributions. It can be seen as a "synthesized coherence function" corresponding to the inverse Fourier transform of the resulting equivalent illumination spectrum Σk_j. For an identical amplitude at each wavelength $\lambda_j=2\pi/k_j$, $T(r_{PQ})$ takes the expression of Eq. (2), with the resulting function plotted in Fig. 1, for 20 wavelengths in the 485–670 nm range equally spaced by Δk in frequency

$$T(r_{PQ}) = \frac{\sin\left(\Delta k r_{PQ} \frac{N}{2}\right)}{\sin\left(\Delta k r_{PQ} \frac{1}{2}\right)}. \tag{2}$$

In Fig. 1, as only a finite number of wavelengths N are used, periodic maxima appears for each OPL Λ

0146-9592/09/050653-3/$15.00

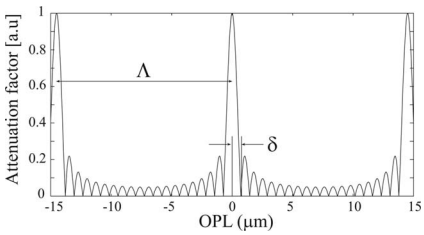

Fig. 1. Nominal filter function $T(r_{PQ})$ for 20 equally k-spaced wavelengths in the 485–670 nm range.

$=2\pi/\Delta k$, also repeating the object image. Obviously, a higher scanned-frequency range $N\Delta k$ gives a better axial resolution $\delta=2\pi/N\Delta k$, and for a given range the higher the wavelength number N the lower the ripples are.

Recently, it has been demonstrated that the filter function ripples can be greatly reduced, at the price of some resolution loss, by the use of a "weighting function" when summing the different wavefronts Ψ_j, e.g., with a Gaussian distribution [13]. In this case, the sum of the different wavefronts is done as in Eq. (3),

$$\Psi(Q)=\sum_{j=0}^{N-1} w_j\Psi_j(Q), \tag{3}$$

with $w(k)$ being the weighting function.

Our experimental setup is depicted in Fig. 2(a), with the laser source being a femtosecond optical parametric amplifier (OPA) delivering 200–250 fs pulses at 250 kHz within a 480–675 nm wavelength tunable range. Motorized OPA wavelength tuning enables about 1 nm/s tuning speed with roughly 1 nm precision, and the temporal coherence length (L_c) given by the pulse width is about 60–75 μm. In Fig. 2(a), the thick BK7 glass block in the reference arm is needed to compensate for dispersion when scanning the wavelength, mainly induced in the object arm by the 1.25 NA 100× microscope objective (MO). The sample is a 90% ethanol-fixed 4 μl blood solution suspended in a HEPA (hepis potassium albumin) buffer held between two 0.17 mm glass coverslips, as shown in Fig. 2(b), where the lower face of the upper coverslip is custom designed with a broadband antireflection (A/R) coating. Combined with the inverted geometry, this ensures that the extremely low signal reflected by the RBC membrane is not lost among an intense glass–water reflection generated at the interface, as both reflectivity are now ideally in a similar range; taking $n_{\text{hemoglobin}}=1.405$ [14] and approximating the HEPA medium index as $n_m=n_{\text{water}}=1.33$ yields about 0.08% reflectivity for the membrane compared to 0.4% for the raw glass–water interface. However, with our custom broadband A/R coating reducing the coverslip-medium reflectivity to less than 0.05%, combined with the low-coherence DHM setup, direct on-cell phase reflection is now possible. Indeed, the preparation thickness is far above L_c, thus the higher intensity reflection from the lower nontreated coverslip does not interfere.

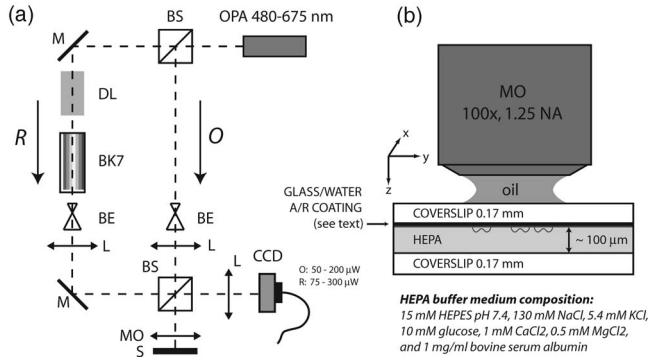

Fig. 2. Experimental configuration. (a) Optical setup. BS, beam splitter; M, mirror; DL, delay line; BK7, BK7 glass block; BE, beam-expander; L, lens; MO, microscope objective; S, specimen. (b) Sample arrangement.

Experimentally, the sample is sequentially illuminated by 20 equally k-spaced wavelengths in the 485–670 nm range. Although this takes theoretically less than 4 min, each hologram acquisition requires a manual shutter time adjustment; thus the overall scanning time is closer to 20 min (optical power precalibration could lower this down to 4 min). Then the complex wavefront is digitally reconstructed [15]. Prior to summation, the different phase offsets φ_j are adjusted for each wavefront in a constant-phase reference plane $z=0$, here the A/R-treated coverslip around the imaged RBC, to avoid random addition [11]. Finally, a phase-only addition is performed as expressed in Eq. (4) for a point $Q(x,y,z)$,

$$\Psi(x,y,z)=\sum_{j=0}^{N-1} w_j\frac{\Psi_j(x,y,0)}{\|\Psi_j(x,y,0)\|}e^{-i\varphi_j}e^{i\varphi_z}, \tag{4}$$

with $\varphi_z=4\pi n_m z/\lambda_j$.

With the used wavelengths and without the weighting function in the sense of Eq. (3) ($w_j=1$), the theoretical tomographic axial resolution of this experiment δ is about 640 nm in the z direction, and the measurement range Λ corresponds to about 12 μm as defined in Fig. 1. However, the lateral ripples in Fig. 1 are still important, with only a −7 dB sidelobe attenuation; thus the effective resolution can be much worse. As in [13], we choose to apply a weighting function to reduce these ripples as described in Eq. (3), but in our case we use the Kaiser function of Eq. (5) (far more efficient than Gaussian windows when dealing with truncated spectra [16]),

$$w(k)=\frac{J_0\left(\alpha\sqrt{1-4\left(\frac{k}{N\Delta k}\right)^2}\right)}{J_0(\alpha)}, \tag{5}$$

with α as a tunable coefficient between 0 and 10 [16].

The Kaiser window of Eq. (5) has the advantage of versatility as one can tailor the function to suit a particular trade-off between ripples and resolution. In this experiment the value $\alpha=3.8$ is chosen as a trade-off resulting in sidelobes suppression of −15 dB and an axial resolution $\delta=1$ μm.

To the extent of our knowledge Figs. 3(a) and 3(b) show thereafter obtained cellular membrane reflec-

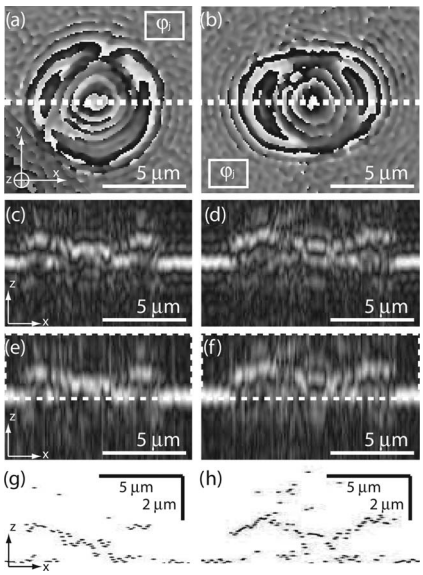

Fig. 3. Results for two different RBCs. (a) and (b) Reflection DHM phase images; (c) and (d) tomographic $X-Z$ cuts through the cell along the dashed curve in (a) and (b) with no weighting function. (e) and (f) Same as (c) and (d) but with an $\alpha=3.8$ Kaiser weighting function; (g) and (h) peak-detected results applied on a zoomed region (white dashed rectangle) of (e) and (f).

tion DHM phase images, in this case of two different RBCs. Then Figs. 3(c)–3(f) compare both the unitary and the Kaiser-weighted $X-Z$ tomographic cut results on a 7.5 μm axial scale with a slice-thickness oversampling of 200 nm. In Fig. 3, one can clearly distinguish the surrounding coverslip surface and the expected biconcave shape of the RBC external membrane, although this kind of cell is only 2–3 μm high. The RBC-coverslip interface signal is weaker as the A/R treatment makes this reflection nearly two times lower than the outer membrane interface with the medium. Even if the unitary window reconstruction of Figs. 3(c) and 3(d) may appear sharp, the strong ripples degrade the effective resolution while the enhanced Kaiser cuts of Figs. 3(e) and 3(f) are significantly less degraded with little resolution loss. Indeed, Figs. 3(g) and 3(h) show high-resolution cuts with a finer 50 nm slices thickness oversampling obtained by a common thresholded local peak-detection algorithm applied along each Z-profile of the ripples-free Kaiser tomography. Figure 4 finally shows the 3D point cloud corresponding to the whole 3D volume resulting from all $X-Z$ cuts, such as Figs. 3(g) and 3(h), thanks to the presented Kaiser ripples attenuation.

In summary, the proposed wavelength-scanned reflection tomography configuration and reconstruction method enables submicrometer-range 3D reconstruction of cells, with enough precision to obtain a direct membrane signal and position detection, with no mechanical scanning. These preliminary results are promising for interferometric and digital holography investigation of cells and cellular structures, e.g., for

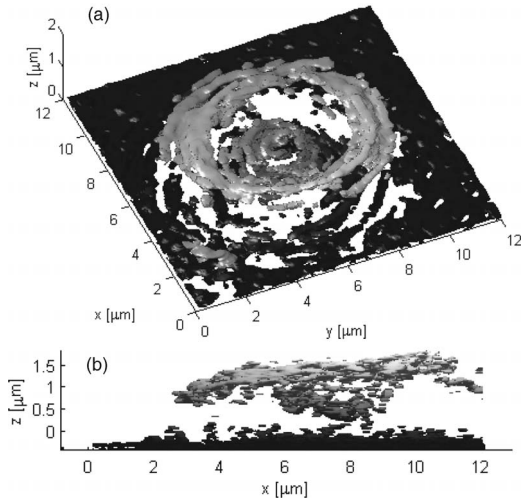

Fig. 4. (a) 3D representation of the series of peak-detected tomographic cuts as in Fig. 3(g) on the RBC of Fig. 3(a); (b) lateral view of (a).

creating models relating the integrated phase signal obtained by these techniques to the volume and true shape of a multilayer specimen.

References

1. P. Marquet, B. Rappaz, P. J. Magistretti, E. Cuche, Y. Emery, T. Colomb, and C. Depeursinge, Opt. Lett. **30**, 468 (2005).
2. G. Popescu, T. Ikeda, C. Best, K. Badizadegan, R. Dasari, and M. Feld, J. Biomed. Opt. **10**, 060503 (2005).
3. B. Rappaz, A. Barbul, Y. Emery, R. Korenstein, C. Depeursinge, P. J. Magistretti, and P. Marquet, Cytometry, Part A **73A**, 895 (2008).
4. B. Kemper, D. Carl, J. Schnekenburger, I. Bredebusch, M. Schafer, W. Domschke, and G. von Bally, J. Biomed. Opt. **11**, 034005 (2006).
5. B. Rappaz, P. Marquet, E. Cuche, Y. Emery, C. Depeursinge, and P. J. Magistretti, Opt. Express **13**, 9361 (2005).
6. B. Rappaz, F. Charrière, C. Depeursinge, P. J. Magistretti, and P. Marquet, Opt. Lett. **33**, 744 (2008).
7. F. Charrière, A. Marian, F. Montfort, J. Kühn, T. Colomb, E. Cuche, P. Marquet, and C. Depeursinge, Opt. Lett. **31**, 178 (2006).
8. W. Choi, C. Fang-Yen, K. Badizadegan, S. Oh, N. Lue, R. R. Dasari, and M. S. Feld, Nat. Methods **4**, 717 (2007).
9. M. Debailleul, B. Simon, V. Georges, O. Haeberlé, and V. Lauer, Meas. Sci. Technol. **19**, 074009 (2008).
10. M. K. Kim, Opt. Express **7**, 305 (2000).
11. F. Montfort, T. Colomb, F. Charrière, J. Kühn, P. Marquet, E. Cuche, S. Herminjard, and C. Depeursinge, Appl. Opt. **45**, 8209 (2006).
12. M. C. Potcoava and M. K. Kim, Meas. Sci. Technol. **19**, 074010 (2008).
13. L. Yu and Z. Chen, Opt. Express **15**, 878 (2007).
14. F. Moritz and M. Martina, J. Biomed. Opt. **10**, 064019 (2005).
15. T. Colomb, E. Cuche, F. Charrière, J. Kühn, N. Aspert, F. Montfort, P. Marquet, and C. Depeursinge, Appl. Opt. **45**, 851 (2006).
16. B. Lathi, *Signal Processing and Linear System* (Berkeley-Cambridge, 1998).